Distinct mobility patterns of BRCA2 molecules at DNA damage sites

Maarten W. Paul[1,*], Jesse Aaron[2], Eric Wait[2,3], Romano M. Van Genderen[1], Arti Tyagi[1,4], Hélène Kabbech[5], Ihor Smal[1,6], Teng-Leong Chew[2], Roland Kanaar[1] and Claire Wyman[1,7]

1 Department of Molecular Genetics, Oncode Institute, Erasmus MC Cancer Institute, Erasmus University Medical Center, Rotterdam, Netherlands

2 Advanced Imaging Center, HHMI Janelia, Ashburn VA, United States

3 Elephas Biosciences, Madison WI, United States

4 Department of Bionanoscience and Kavli Institute of Nanoscience Delft, Delft, University of Technology, Delft, Netherlands

5 Department of Cell Biology, Erasmus University Medical Center, Rotterdam, The Netherlands

6 Theme Biomedical Sciences, Erasmus University Medical Center, Rotterdam, Netherlands

7 Department of Radiation Oncology, Erasmus MC Cancer Institute, Erasmus University Medical Center, Rotterdam, Netherlands

* To whom correspondence should be addressed. Tel+31 10 7043158; Email: m.w.paul@erasmusmc.nl

ABSTRACT

BRCA2 is an essential tumor suppressor protein involved in promoting faithful repair of DNA lesions. The activity of BRCA2 needs to be tuned precisely to be active when and where it is needed. Here, we quantified the spatio-temporal dynamics of BRCA2 in living cells using aberration-corrected multifocal microscopy (acMFM). Using multicolor imaging to identify DNA damage sites, we were able to quantify its dynamic motion patterns in the nucleus and at DNA damage sites. While a large fraction of BRCA2 molecules localized near DNA damage sites appear immobile, an additional fraction of molecules exhibits subdiffusive motion, providing a potential mechanism to retain an increased number of molecules at DNA lesions. Super-resolution microscopy revealed inhomogeneous localization of BRCA2 relative to other DNA repair factors at sites of DNA damage. This suggests the presence of multiple nanoscale compartments in the chromatin surrounding the DNA lesion, which could play an important role in the contribution of BRCA2 to the regulation of the repair process.

INTRODUCTION

The activity of proteins needs to be controlled spatially and temporally. This is especially true for proteins that maintain the integrity of the genome through DNA repair reactions. These proteins must act at the right time and place to repair DNA damage. They need to cooperate or compete with many other proteins at the same genomic location, such as proteins involved in replication and transcription. The critical parameters that define the activity of these proteins in cells are their concentration and their diffusion rate. Simultaneously, both transient, non-specific and specific interactions determine their spatial organization. These specific and non-specific interactions can be with other proteins but also with other biomolecules such as DNA and RNA.

BRCA2 is an essential DNA repair protein that is present in a low concentration in the cell nucleus. It is found in a complex with several other DNA repair proteins, such as PALB2 and RAD51, which are all required at sites of DNA damage lesions repaired by homologous recombination (1). The central function of BRCA2 is to exchange the single-strand DNA binding protein complex RPA with RAD51 on the resected DNA ends of DNA double-strand breaks (DSB). Additionally, the resolution of stalled replication forks and of interstrand-crosslinks by homologous recombination requires localized activity of BRCA2 at damage sites (2, 3). As an important tumor suppressor, BRCA2 is an extensively studied protein, where BRCA2 mutations are associated with hereditary breast and ovarian cancer (4). However, the biophysical properties of BRCA2 that drive its function in cells are not fully understood. Here, our objective is to define the dynamic behavior of BRCA2 around DNA lesions to understand the critical parameters that are required for BRCA2 to act properly.

DNA-associated proteins can exhibit different modes of diffusion that contribute to their different functions (5, 6). For example, recently it has been reported that the transcriptional regulator CTCF maintains transient binding zones within the cell nucleus, which could be a mechanism to improve its target search efficiency in the nuclear volume (7). Although many nuclear proteins, such as transcription factors, are involved in direct and specific interactions with DNA (sequence motifs, specific structures), it appears that BRCA2 does not depend on this type of interaction for its immobilization at damage sites, but rather on (transient) protein-protein interactions (8). The immobilization and accumulation of BRCA2 is essential for its function, but what interactions are relevant for this behavior and how this correlates

with its function is largely unknown. Several reports indicate a crucial interaction between BRCA2 and PALB2, and indeed BRCA2 accumulation at damage sites depends on the interaction with PALB2 (9), whereas localization of PALB2 itself is influenced by BRCA1 (10) and the ubiquitin ligase RNF168 (11). Recent data suggests that PALB2 chromatin interaction depends on chromatin associated proteins (12, 13), hence those chromatin interactions could also contribute to the diffusive patterns that have been observed for its binding partner BRCA2 (8, 14).

BRCA2 accumulates at DNA damage into so-called foci, like several other homologous recombination repair proteins. It is not yet fully understood how redistribution occurs and how BRCA2 proteins organize themselves at damage sites. In this study, we applied 3D single-molecule multiplane imaging to define the quantitative behavior of endogenous BRCA2 at fluorescently marked DNA damage sites. This revealed that at DNA damage sites, immobilization of BRCA2 increases, but also that those molecules that diffuse near DNA lesions do so with increased confined mobility. Quantification of the number of BRCA2 molecules in the nucleus and at damage sites indicated that only tens of BRCA2 molecules are present per focus, while super-resolution microscopy confirmed the localization of BRCA2 in nanoscale clusters within foci.

MATERIAL AND METHODS

Cell culture

Mouse ES cells were maintained on 0.1% gelatin (Sigma) coated plates in mouse ES cell medium (DMEM, 40% BRL-conditioned medium, 10% FCS (Capricorn Scientific), supplemented with pen-strep, non-essential amino acids (Lonza) and leukaemia inhibitory factor (1000 U/ml) and 0.1 mM β-mercaptoethanol). For the ac-MFM experiments cells were maintained for several passages prior to the experiments in DMEM Knockout medium (Thermofisher) supplemented with 10% FCS (Sigma, F2442), pen-strep, LIF, NEAA and 0.1 mM β-mercaptoethanol. mES cells expressing BRCA2-HaloTag previously generated and described in (1). Mouse ES cells expressing BRCA2-EGFP were previously generated and described in (2).

92 **DNA constructs**

93 The EGFP-tr53BP1 construct was assembled using Gibson Assembly with a fragment of
94 human 53BP1 (amino acids 1221-1709, Addgene #69531) (4) that was cloned in a EGFP
95 Piggybac vector (3).

96 **Generation of cell lines**

97 The EGFP-53BP1trunc Piggybac vector was transfected in BRCA2-HaloTag cells together with
98 the CMV-Hypbase Piggybac transpose plasmid using Lipofectamine 3000 according to the
99 manufacturer's protocol. Cells were selected with puromycin for 1 week after which the
100 selected population was used for the experiments.

101 **Sample preparation of live cell imaging**

102 Between 20,000 and 40,000 cells were seeded the day before the imaging experiment on 8-
103 well ibidi dishes coated with 25 µg/ml laminin (Roche, 11243217001). When indicated, cells
104 were treated with 1 µg/ml mitomycin C (Sigma, M0503). For HaloTag labeling, the medium
105 was replaced and, subsequently, the cells were labeled with 50 nM JF549-HaloTag dye,
106 unless a different concentration is indicated, followed by washing with PBS and replacement
107 with fresh medium. Imaging was done in FluoroBrite DMEM medium (ThermoFisher,
108 A1896701) complemented with 10% FCS, pen-strep, LIF, NEAA, 0.1 mM β-mercapto-ethanol.

109 For FRAP experiments cells were labelled with 250nM of JF549-HaloTag ligand and cells were
110 labelled and washed as described above. For 2D tracking experiments in wild-type and
111 53bp1 knockout cells, cells were labeled with 0.5 nM JFX549 for 10 minutes.

112 **Sample preparation for immunofluorescence**

113 The cells were grown in 8-well glass bottom dishes (Ibidi) or 24 mm round coverslips (#1.5H,
114 Marienfeld, 0117640), coated with laminin as described above. For fixation cells were washed
115 with PBS once and fixed with 4% PFA (Thermo-Fisher) in PBS for 10 minutes. Cells were
116 washed with PBS with 0.1% triton for 3 times followed by two 10-minute washing steps. Cells
117 were blocked with 3% BSA in PBS for 20 minutes followed by incubation of the primary
118 antibodies in blocking buffer. After washing with PBS with 0.1% Triton, cells were incubated
119 with fluorescently labeled secondary antibodies for 1 hour at room temperature.

120 For immunostaining of 53BP1 a rabbit polyclonal antibody was used (1:1000, Novus
121 biologicals, NB100-304) together with anti-rabbit F(ab')2 fragment conjugated with CF568
122 (1:1000, Sigma, SAB4600310).

123 For dSTORM imaging of HaloTag protein fusions, cells were incubated with 500 nM AF647-
124 HaloTag ligand (kind gift from Luke Lavis) together with the primary antibodies in blocking
125 buffer for 2 hours at room temperature.

126 For STED imaging, mES cells expressing BRCA2-EGFP (2) were treated with Mitomycin C (1
127 µg/ml) for 2 hours. Subsequently, the cells were fixed 2 hours later with 4 % PFA. Cells were
128 immunostained as described above using anti-GFP nanobody conjugated with STAR635P
129 (1:500, FluoTag X4, 0304-Ab635P, NanoTag). 53BP1 was visualized with anti-53BP1 antibody
130 (1:2000, Novus Biologicals, NB100-304) and secondary anti-rabbit Alexa594 (1:2000,
131 ThermoFisher). Samples were mounted in ProLong Gold mounting medium on object
132 glasses.

133 **Microscope setup and image acquisition**

134 *Ac-MFM setup* The ac-MFM system was as described by Abrahamson et al (5). In summary,
135 specimens were imaged on a Nikon TiE epifluorescence microscope with a 100x 1.45NA Plan
136 Apo objective lens (Nikon) and illuminated by 3-6kW/cm^2 561 nm laser excitation.
137 Fluorescence was collected and passed through a custom multifocal grating and color
138 correction grating as described by Abrahamsson et al. Nine focal planes were imaged onto
139 two EMCCD detectors (iXon DU897, Andor) with a frame rate up to 30 Hz. The focal position
140 of the microscope was maintained by active stabilization.

141 Every day, prior to the imaging experiments, a sample with mounted 100 nm Tetraspeck
142 beads (ThermoFisher) was used to correct for chromatic aberrations, to measure the z-slice
143 separation distance, to determine relative z-plane detection efficiency, and to align image
144 channels. A Tokai Hit microscope stage holder was used to maintain cells at 37C with 5%
145 CO_2. Movies of 2000 frames were recorded, where in every 50th frame the GFP signal was also
146 recorded on the second camera detector. The sample was continuously illuminated with
147 561nm light and constant low 405 nm light for photoactivation of Halo-JF549.

148 *Confocal imaging and FRAP* Experiments were conducted on a Zeiss Elyra PS1 system with a
149 Tokai Hit stage incubator calibrated at 37 ºC and 5 % CO_2 using a 63x objective (NA 1.4 Plan
150 Apo). For both FRAP experiments (**Figure 1**) and quantitative confocal experiments (**Figure**
151 **3**) a GaAsP detector was used. FRAP experiments were acquired using a square ROI of
152 1.14x1.14 µm, which was scanned at a 0.2 s interval, with 20 frames before bleaching, 4
153 frames bleaching at full laser power, followed by 230 frames to record recovery. Cells that
154 moved too much during acquisition were excluded from the analysis. Mean intensity from
155 the bleach ROI was measured over time. The intensity traces were normalized by the mean
156 intensity of frame 10-20 before bleaching. The data in **Figure 1A** shows the average
157 normalized intensity trace of multiple experiments, whereas the shading represents the
158 standard error of the mean intensity.

159 *dSTORM* Imaging was performed using a Zeiss Elyra PS1 system using a 100x 1.46NA Korr α
160 Plan Apochromat objective. 561 and 642 100mW diode lasers were used to excite the
161 fluorophores together with respectively a BP 570–650 + LP 750 or LP 655 excitation filter.
162 dSTORM imaging was performed using near-TIRF (HiLo) settings, while the images were
163 recorded on an Andor iXon DU 897, 512x512 pixel EMCCD camera.

164 For drift correction and channel alignment 100 nm Tetraspeck beads (ThermoFisher) were
165 added to the sample. To perform dSTORM imaging, an imaging buffer was prepared
166 containing 40 mM MEA (Sigma), 0.5 mg / ml glucose oxide (Sigma), 40 µg/ml Catalase
167 (Sigma) and 10% w / v glucose in Tris pH 8.0. dSTORM images were acquired sequentially,
168 starting with Alexa 647 staining followed by CF568 imaging. At least 10,000 images were
169 acquired at an interval of 33ms per frame.

170 The raw data was analysed by ZEN software. The molecules were localized, and a drift
171 correction was applied using image correlation in the two images separately. Localizations
172 that were present within 20 nm of each other in the 5 subsequent frames were grouped.
173 Subsequently, the two images were combined, and the channels were aligned laterally using
174 100 nm Tetraspeck beads that are deposited into the sample.

175 For blinking correction of the plots in **Figure S8** we made use the pairwise distance
176 distribution correction algorithm (DCC) (6). ROIs with ungrouped localizations were loaded

177 into Matlab and processed with the DCC script taking into account the photon counts as
178 obtained from the ZEN software.

179 *STED* The samples were imaged on a Leica SP8 tauSTED. Star635 signal was excited with a
180 white-light laser tuned at 632 nm and 775 nm depletion laser with a 2D STED depletion
181 pattern, whereas Alexa594 was imaged with the same depletion laser, but excited with the
182 white light laser tuned at 561 nm. STED images were deconvolved using Huygens software
183 (SVI).

184 **Image analysis for ac-MFM**

185 Raw images from the ac-MFM microscope were converted to 3D stacks and corrected for
186 chromatic aberrations in MATLAB (https://github.com/aicjanelia/MFM) and processed using
187 background subtraction and Richardson-Lucy deconvolution (7px rolling ball, 5 iterations,
188 respectively). Subsequently, molecules were localized and tracked in 3D using the TrackMate
189 plugin (7) in ImageJ after pre-processing using and Gaussian blur denoising (0.7px radius).
190 The molecules were linked at a maximum frame-to-frame distance of 500 nm.

191 EGFP-tr53bp1 movies, that were used to define the DNA damages sites, were processed in
192 Matlab, where frames were identified that contained EGFP signal, the signal in intermediate
193 frames was interpolated linearly based on the image frame before and after. The foci signal
194 was identified using Laplacian of Gaussian edge detection and a binary mask was created.

195 Next, for every point of the tracks it was determined whether it was in or outside the mask.
196 To compare the results to a random situation, data sets were generated by randomly
197 redistributing the identified 3D objects at the first frame of the movie, along the x-y axes in
198 the image plane within the convex hull surrounding the centre of mass of all foci. The
199 MATLAB routines used for the analysis can be found in

200 https://github.com/maartenpaul/MFManalysis_Matlab/ (based on original code repositories:
201 https://github.com/aicjanelia/MFM and https://gitlab.com/aicjanelia/visitor-maarten-paul).
202 Subsequently a script in R was used for processing of the tracks and plotting of the data
203 (https://github.com/maartenpaul/MSDanalysis_MFM). Python code to segment the tracks
204 into different mobile states using deep learning and to estimate the mean square

displacement and moment scaling spectrum of the individual tracklets (8) was incorporated into Rstudio using the reticulate package (9).

For further analysis, track(let)s presenting at least one frame of their lifetime inside the mask were considered associated with the DNA damage sites.

The angle (θ) between two displacements within the track(let)s was calculated as described in Hansen (2019) (7). For the angle analysis displacements, immobile tracklets and x-y displacements below 100 nm were excluded from the analysis.

For a single track(let) with $r(t) = (x(t), y(t))$ its coordinates and $T \geq 8$ its total track length, the mean squared displacement (MSD), at different time lags Δt, was computed as follow:

$$\mathrm{MSD}(\delta\Delta t) = \frac{1}{T-\delta}\sum_{i=1}^{T-\delta}|r(t_i) - r(t_i + \delta)|^2 \quad (1)$$

The apparent diffusion constant D_{app} and anomalous exponent α were estimated by fitting a linear regression on the logarithm form of the MSD power-law equation (10) (using the first 4 MSD fitting points):

$$\mathrm{MSD}(\Delta t) \sim 2nD_{app}\Delta t^{\alpha} \quad (2)$$

where n is the number of dimensions.

The radius of confinement $R_c = R_\infty\sqrt{(n+2)/2}$ was measured after estimating the plateau R_∞ of the MSD curve (11). The latter was estimated by fitting the following equation, using the first 20 MSD fitting points and the "curve_fit" function from the Python SciPy library:

$$\mathrm{MSD}(\Delta t) \sim R_\infty^2\left(1 - e^{-2nD_{app}\Delta t/R_\infty^2}\right) + 4\sigma^2 \quad (3)$$

with σ^2 the experimental noise level.

Image analysis dSTORM

For quantification of BRCA2 clusters, 53BP1 foci were identified by applying an Otsu threshold on 53BP1 images and saved as ImageJ ROIs. The ROIs were imported in R and BRCA2 localizations that are within the ROIs were clustered using the RSMLM package using the ToMaTo clustering algorithm (r=50, threshold=0.1) (13). To remove spare localizations clusters with less than 5 localizations were filtered out. Shape features describing these clusters were determined using the SMoLR package (14). The size of clusters is defined as the mean of the FWHM of the major and the minor axis of the localizations within the cluster.

235 The distance between the clusters is determined as the distance between the centre of mass
236 of the two clusters within the same segmented 53BP1 focus.

237 **Quantification of cellular concentration of BRCA2**

238 HaloTag-GST (61 kDa) (Promega, G4491) was labelled with JF646 for 4 hours at 4 ° C on ice
239 with 3x excess HaloTag ligand (buffer: 1x PBS, 20% glycerol, 1 mM DTT). Followed by removal
240 of the unreacted HaloTag ligand using a Zeba desalting column (7K MWCO, 0.5 ml,
241 ThermoFisher, 89882). Using SDS-PAGE it was confirmed that the labelled protein was
242 recovered after labelling and elution from the column. The concentration of the labelled
243 protein was validated using Nanodrop and on SDS-Page using a BSA with known
244 concentration. Subsequently this labelled protein was used as reference to estimate the
245 amount of BRCA2 per cell.

246 The nuclei of live cells were segmented in 3D using a routine in TrackMate (12), which uses
247 Stardist (15) for 2D segmentation of nuclei, followed by connecting the matching nucleus
248 segmentation in the 3D image stack. A 3D label image was exported and used in a custom-
249 made routine developed in CellProfiler (16). The label image was used to generate 3D nuclei
250 objects and was used to determine the nuclear volume and integrated intensity of the
251 BRCA2-halotag intensity. The BRCA2 foci were segmented using an adaptive threshold in 3D
252 and volume and intensity were measured. The CellProfiler pipeline and accompanying R
253 code for processing and plotting the data is available at
254 https://github.com/maartenpaul/Halo_cell_quant .

255 The integrated intensity (a.u.) was converted to concentration and number of molecules by
256 comparing the intensity to a titration curve of the labelled HaloTag-GST::JF646 standard
257 protein. Using this titration curve the intensity per pixel can be converted to the local
258 concentration of HaloTag protein. Assuming that the segmented nuclei are much larger than
259 the confocal volume per pixel this conversion can be used to estimate the concentration of
260 BRCA2 in the nuclei. Subsequently, the concentration can be converted to number of
261 molecules per nucleus by dividing the volume and Avogadro's number.

262 For in-gel analysis of in vivo labelled BRCA2-HaloTag, HaloTag was labelled with JF646-
263 HaloTag ligand in live cells grown on plates. Subsequently cells were trypsinized and the cell

264 concentration was determined. Cells were resuspended at 25,000 cell/µl and treated with
265 benzonase in buffer with protease inhibitors (2 mM MgCl2, 20 mM Tris pH 8, 10% glycerol,
266 1% triton X-100 and 25 U/ml benzonase) and subsequently lysed by adding 2x Laemmli
267 buffer without bromophenol blue, at equal volume. Cell lysates were run on 3-8% SDS-Page
268 Tris-Acetate gel. The fluorescently labelled proteins were imaged in the gel using a Typhoon
269 gel imager (Amersham).

270

271 **RESULTS**

272 Previous studies have shown, that BRCA2 appears more immobile after induction of DNA
273 damage (8, 14). However, those studies did not investigate the spatial distribution of
274 immobilized BRCA2 after induction of DNA damage. BRCA2 is involved in the repair of
275 different types of lesions that also involve RAD51-mediated homology recognition and DNA
276 strand exchange. One type of lesion requiring BRCA2 for repair is the interstrand-crosslink,
277 which can be induced by chemical reagents such as mitomycin C. The formation of BRCA2
278 foci after mitomycin C treatment is correlated with the observation that BRCA2 becomes
279 more immobile and suggests that induction of DNA damage causes a redistribution of
280 BRCA2 to DNA damage sites (14). In this study, we use a previously generated mouse
281 embryonic stem (ES) cell line, in which endogenous BRCA2 is homozygously tagged with a
282 HaloTag by knock-in mediated by CRISPR / Cas9. This enables direct, real-time visualization
283 of individual BRCA2 molecules in living cells. Here, we used this cell line (as described in Paul
284 et al., 2021) to investigate the mobility of BRCA2 at damage sites by applying spot-FRAP at
285 BRCA2-HaloTag mitomycin C-induced DNA repair foci. These experiments show a large
286 immobile fraction of BRCA2 at the damage sites, with a 44% fluorescence recovery of the
287 prebleached signal during 50 seconds of data acquisition, corrected for the residual
288 fluorescence signal after photobleaching. (**Figure 1A**). This large immobile fraction for
289 BRCA2 is not observed in the nucleoplasm outside the foci, although the low concentration
290 of BRCA2 in the cell nucleus makes these measurements challenging. Together, our FRAP
291 experiment suggests that upon induction of DNA damage, part of the BRCA2 molecules
292 remain associated to DNA damage sites.

293 **3D single-molecule tracking reveals BRCA2 immobilization at individual DNA repair**
294 **foci**

295 Although FRAP is a powerful technique for studying the dynamic exchange of proteins in
296 cells, it has limited possibilities to differentiate between different types of diffusive behavior
297 of proteins at the single-molecule level, which can be better investigated with single-
298 molecule tracking (15). In this study, we applied 3D single-molecule tracking in the entire
299 nucleus using a multicolor aberration-corrected multifocus microscope (acMFM) (16) (**Figure**
300 **1B, Movie S1**). Single-plane single-molecule tracking is restricted by the imaging volume,

301 since molecules can move in and out of the focal plane. Although the axial excitation
302 thickness for HiLo illumination acquisition is in the range of 1-2 µm, the cell nucleus is about
303 5 µm thick. Furthermore, DNA repair foci, in which BRCA2 dynamics needs to be quantitated,
304 are distributed across the entire nuclear volume, and therefore it is not possible to capture all
305 foci in one focal plane, and hence some of the foci will be out of focus. Finally, both cell
306 nuclei and DNA repair foci are dynamic in their composition and spatial location within the
307 nucleus (17, 18); therefore the regions from which data should be recorded are moving
308 during image acquisition.

309 Using an acMFM microscope, nine focal planes are projected (approximately 400 nm
310 spacing) on a single camera chip. This allows for rapid instantaneous 3D imaging at 9 planes.
311 To identify DNA damage, EGFP-tr53BP1 was introduced into cells as a marker of DNA breaks.
312 This construct expressing a fragment of the 53BP1 protein (a.a. 1221-1709) is a useful marker
313 for DNA breaks and was previously validated to not interfere with the repair process (19–21).
314 Immunofluorescence experiments confirmed the proper localization of the tr53BP1 protein in
315 our cells, overlapping with the signal of endogenous 53BP1. Upon treatment with the DNA
316 crosslinking agent mitomycin C, tr53BP1 foci can be observed that co-localize with BRCA2
317 accumulations (**Figure S1**). By applying 3D single-molecule tracking and simultaneously
318 following the foci distribution in cells, we directly correlate the diffusive behavior of BRCA2
319 with regions of DNA damage (**Figure 1C**). This developed image analysis routine allows us to
320 identify whenever a single BRCA2 molecule is within a region of damage during image
321 acquisition. Subsequently, we tracked the localized molecules in 3D and compared their 2D
322 and 3D displacements inside and outside the mask (**Figure 1D**). This comparison of
323 displacement distributions shows a distribution with shorter displacements inside the mask
324 compared to outside of the mask (**Figure 1E,F**). To validate the observed differences in the
325 displacements between inside and outside the DNA repair foci, we also analyzed the data
326 after randomly redistributing the segmented foci objects along the x- and y-axes of the
327 image plane (see Methods section for details). Compared to the original data, the
328 randomized data shows no difference in the distribution of displacements inside compared
329 to outside the foci (**Figure 1E,F** bottom panels). Additionally, we quantified the number of
330 localizations in the mask and observed that 9.9% of the localizations are within the mask
331 whereas the randomly defined mask contains 1.3% of the localizations. This shows that there

332 is a 7.9 times enrichment of localizations in the data compared to the random mask,
333 confirming the observation that BRCA2 accumulates at foci containing 53BP1 (**Figure 1G**).

334 Using the described approach, we investigated the motion patterns of BRCA2 specifically at
335 DNA damage. We define molecules to be inside of the focus if they reside at least one frame
336 (50 ms) inside the 53BP1 defined focus volume. This definition allows for comparison of
337 tracked molecules that are inside or in close proximity of the foci, with tracks outside the
338 foci, without introducing edge effects caused by using a binary mask: immobile molecules
339 will have a higher chance of staying within the mask for a longer time and hence will be
340 identified more frequently if we would do the analysis where the entire track needs to be
341 inside the mask. Since we have previously observed that BRCA2 molecules can frequently
342 switch between different diffusive states, we applied a recently developed deep learning
343 approach method to our single-molecule tracking data to segment tracks into tracklets (22).
344 With this method we could define three different diffusive states for BRCA2: fast (D_{app}=0.44
345 $\mu m^2/s$), slow (D_{app}=0.05 $\mu m^2/s$) and immobile (D_{app}=0.01 $\mu m^2/s$), comparable to previous
346 studies (8, 14, 22). For each individual tracklet (see **Figure S2** for the distribution of track
347 lengths), we fitted the mean square displacement (MSD) to a power-law equation (MSD ~ t^{α})
348 permitting the extraction of the anomalous exponent α, a metric that gives an indication of
349 the diffusion mode of the track with $0 < \alpha < 1$ showing specifically subdiffusion, and $1 < \alpha <$
350 2 superdiffusion. All molecules exhibited an anomalous exponent α below 1 suggesting
351 subdiffusion. Furthermore, both immobile (α=0.34) and slow molecules (α=0.60) display
352 more subdiffusive motion compared to fast molecules (α=0.92) (**Figure 2A**). When
353 comparing different MSD curves for each diffusive state, we observe a clear separation
354 between the states, indicating three distinct mobility patterns. This observation is confirmed
355 by the theoretical MSD curves plotted using the median values in **Figure 2B**.

356 Subsequently we compared the diffusion constant D_{app} and the anomalous exponent α of
357 the tracklets in and outside the foci. The diffusion constant of the different fractions is not
358 affected (**Figure 2C**). However, the measured anomalous exponent α is reduced for all
359 fractions within the focus. Quantification of the fraction of tracklets inside the mask shows a
360 clear enrichment in the amount of BRCA2 tracklets in the immobile state at the identified
361 DNA damage sites (42 to 60%), while both the slow (32 to 22%) and fast fraction (26 to 19%)
362 did decrease (**Figure 2D**).

363 Finally, we compared the results of cells treated with mitomycin C with untreated cells
364 (**Figure S3**). In untreated mouse ES cells, spontaneous foci can be observed and
365 immobilization of BRCA2 has also been observed under unchallenged conditions, although
366 to a lesser extent. We confirmed these observations in our current experiments, where in the
367 untreated cells we see that the immobile fraction inside (52% versus 60%) is lower while the
368 immobile fraction outside the foci is comparable (38% versus 39%) to the treated cells. The
369 median diffusion constant of the different fractions was not different compared to the cells
370 treated with mitomycin C. Similarly, to treated cells the value of α was reduced for diffusing
371 fractions inside the foci (**Figure 2, S3**). Interestingly, also the fraction of BRCA2 molecules
372 that resides in 53BP1 foci is lower compared to treated cells (3.4% versus 9.9%), indicating
373 that at spontaneous foci less BRCA2 molecules accumulate.

374 **Diffusive BRCA2 molecules exhibit enhanced subdiffusive motion at DNA repair foci**

375 Our aim was to further investigate the mechanism by which BRCA2 accumulates at the
376 damage sites. Tracking analysis showed that at sites of DNA damage, next to an increased
377 immobile fraction, slow diffusing molecules exhibited subdiffusive diffusion (alpha<1). An
378 alternative approach to study the subdiffusion of proteins in cells is to look at the angular
379 distribution, a sign of anisotropic motion of the tracked molecules. Molecules that exhibit
380 regular diffusion will move in a random direction independent of their previous position, but
381 when motion is confined, molecules are more likely to make a backward step than forward
382 with respect to the previous step (5, 7). To investigate only diffusive molecules, we excluded
383 tracklets that are assigned by our state segmentation method as immobile from the analysis.
384 In fact, after calculating the angles, mobile BRCA2 molecules appear to have an anisotropic
385 motion pattern, and this anisotropy is enhanced at the DNA repair foci (**Figure 2E**). This is
386 the case for both slow and fast diffusing molecules, although the fastest diffusing molecules
387 show this behavior to a lesser extent (**Figure 2F**). Subsequently we quantified the fold
388 increase in the backward angle (180 +/- 15 degrees) versus the forward angle (0 +/- 15
389 degrees) compared to the average displacement of the tracked molecule at that time (**Figure
390 2G**). We can observe a peak between 80 and 150 nm of the average displacement, which
391 suggests that, especially molecules having shorter displacements, are, transiently, more
392 confined to a subregion of the focus. Then we quantified the distribution of displacements of
393 molecules that transition from inside to outside or vice-versa. We observe that for both

394 transitions the smaller displacements are observed compared to the random mask (**Figure**
395 **2H**). However, the transitions in either direction appear similar for both the data set and the
396 random mask, suggesting that movement in and out of the focus is not restricted.

397 To evaluate whether the BRCA2 molecules inside the foci do display confined motion within
398 the repair focus, we fitted the mean-square-displacement data to a confined motion model
399 which estimates a radius of confinement R_c. For all immobile tracklets localized inside or
400 outside the mask, we estimated the plateau of each averaged MSD line (**Figure S4**). The
401 results show an estimated R_c of about 0.126 µm outside the foci and 0.144 µm inside the foci
402 (versus 0.136 µm inside the randomly generated mask). We reproduced the same
403 measurements for the moving molecules (slow and fast combined), although the motion is
404 less confined regarding the previously calculated α values, leading to a potential delayed
405 MSD plateau. We found a R_c value of 1.57 µm outside and surprisingly a very large Rc value
406 of about 6.21 µm inside the foci (versus 2.70 µm inside the random masks). Although the
407 curve fits well to the data, the lack of a clear plateau in the MSD curve suggests that, for the
408 slow and fast diffusing molecules, the molecules do not experience confinement correlating
409 with focus size. For comparison we also fitted the same MSD curves to an anomalous
410 diffusion model which displays a non-linear relation between displacement and time, but
411 without constraint or a boundary (**Figure S5**). This also resulted in a good fit of the data
412 suggesting that the motion of BRCA2 at repair foci can be explained by transient binding of
413 molecules within the damage site resulting in the observed anomalous diffusion patterns.

414 **BRCA2 is localized in multiple clusters of several BRCA2-molecules at DNA repair foci**

415 To better understand the organization of BRCA2 in the foci, we have applied dSTORM
416 imaging of BRCA2-Halo to visualize the spatial arrangement of BRCA2 under similar
417 experimental conditions in 53BP1 foci after mitomycin C treatment. Previous experiments in
418 human cells using anti-BRCA2 antibodies showed the presence of multiple BRCA2 clusters
419 per focus (23). By using direct HaloTag labelling of BRCA2-Halo with Alexa647-HaloTag
420 ligand, we can now more accurately localize BRCA2 in foci by single-molecule localization
421 microscopy. We used 53BP1 foci to identify regions of interest to determine the localization
422 of BRCA2 within. Visual comparison of the localization of 53BP1 and BRCA2 in the foci
423 indicates that BRCA2 is frequently excluded from regions that are dense in 53BP1 signal

424 (**Figure 3A**). Within the 53BP1 foci we quantified BRCA2 to localize in multiple small clusters
425 of about 50 nm in size (**Figure 3A-C**). Furthermore, we quantified the distance between
426 BRCA2 clusters (Figure 3D). This analysis shows that most BRCA2 clusters are most frequently
427 200 nm spaced apart with respect to their centre of mass. To confirm that BRCA2 cluster
428 formation was present in cells in lateS/G2, where BRCA2 is expected to contribute to
429 homology-directed repair, we applied dSTORM imaging in cells that were labeled shortly
430 with EdU prior to fixation (**Figure S6**). In addition to the differential location between BRCA2
431 and 53BP1, we also identified that RPA is differentially localized in the repair foci with respect
432 to BRCA2 (**Figure S7**).

433 We validated that the inhomogeneous localization that we observed by dSTORM is unlikely
434 to be an artifact caused by repetitive photoblinking, which is known to cause apparent
435 clustering in dSTORM imaging. First we used an algorithm to correct for blinking artifacts
436 and reconstruct the true emitters in a few of the foci (24). This showed that after blinking
437 correction the BRCA2 clusters are still visible (**Figure S8**). Furthermore, we also used 2D-STED
438 imaging of BRCA2 and 53BP1 to determine the super-resolution localization of BRCA2. While
439 the lateral resolution of STED is lower, hence less details are visible it is not affected by
440 blinking artifacts like in dSTORM. With STED imaging we also observe that molecules are
441 differentially organized and that BRCA2 can form multiple clusters per 53BP1 focus (**Figure**
442 **S8**).

443 Subsequently, we wanted to estimate the concentration of BRCA2 in mouse ES cell nuclei to
444 correlate the amount of BRCA2 present at repair foci with the clusters that are present in the
445 foci. For this purpose, we imaged live BRCA2-HaloTag cells by confocal microscopy, while
446 titrating known concentrations of JF646-labeled GST-HaloTag protein in cell culture medium.
447 This allowed us to determine the correlation between voxel intensity and HaloTag protein
448 concentration in the images (**Figure 3E, Figure S9**). Although we did not estimate the actual
449 excitation confocal volume of a voxel, we were able to determine the local concentration of
450 BRCA2-Halo per pixel. With the assumption that the nuclei and foci are larger than the
451 confocal volume, we can use the integrated intensity of the objects to estimate the local
452 concentration and total number of BRCA2 molecules in individual nuclei. This shows a
453 nuclear concentration of 10 nM or about 5,000 molecules per cell nucleus (**Figure 3F**).
454 Additionally, we were able to segment individual BRCA2 foci to estimate the number of

455 BRCA2 molecules per focus. This analysis indicates that the local concentration of BRCA2 is
456 nearly 10 times higher within repair foci (~100 nM) whereas the mean number of BRCA2
457 molecules per focus was estimated at approximately 25 (**Figure 3G**). This increase in
458 concentration of BRCA2 molecules at the repair foci is comparable to increased number of
459 localizations within repair foci we observed with single-molecule tracking (**Figure 1G**). The
460 concentration of BRCA2 we determined in cells is consistent with the quantification of the
461 amount of cellular BRCA2-Halo protein labelled with JF646 and on SDS-PAGE, while using
462 the GST-HaloTag protein with defined concentration as reference (**Figure S9**). Quantification
463 of the total intensity of the protein bands normalized to the number of cells in the sample
464 loaded, reports the average number of BRCA2 molecules per nucleus.

465 **DISCUSSION**

466 In this study we have investigated the dynamic behavior of BRCA2 specifically at 53BP1 foci
467 induced by the DNA crosslinker mitomycin C. Instantaneous multiplane two-color imaging
468 allowed us to detect the BRCA2 molecules localized in DNA repair foci and study their
469 mobility. Previous single-molecule tracking studies of BRCA2 have shown an increase in the
470 immobile fraction of BRCA2 after DNA damage induction (8, 14). Here, we show that this
471 immobilization is caused by BRCA2 that is localized to DNA repair foci. We identified that
472 only about 10% of the BRCA2 molecules that were tracked within the nucleus were
473 accumulated at the foci, which explains the subtle increase in the immobilization of BRCA2
474 measured throughout the nucleus, as we have previously observed. In depth-analysis of the
475 3D tracking data revealed that next to the increased immobilization, diffusing BRCA2
476 molecules inside the foci show increased anomalous diffusion. This anomalous diffusion is
477 most evident in slow moving BRCA2 molecules, with an increased confinement for molecules
478 moving between 80 and 150 nm in a 50 ms time interval. A similar pattern of anomalous
479 diffusion is observed for BRCA2 molecules outside the foci, but to a lesser extent (Figure 2E-
480 G). Similar motion patterns have been observed for other nuclear proteins such as CTCF and
481 transcription factors (Sox2 and Oct4) (6, 7, 27), which contribute to the function of these
482 proteins, such as improved target search in chromatin. For BRCA2 complexes, this could be a
483 mechanism to efficiently probe the chromatin environment for the presence of DNA
484 damage. The difference in the chromatin environment (*e.g.,* changes in specific histone
485 modifications) present at DNA damage sites could enhance transient binding of BRCA2

486 complexes at the damaged chromatin. This will allow BRCA2, even at its low concentration,
487 to dynamically associate with the damaged genomic region. This local difference in affinity
488 could serve as a mechanism to retain and concentrate BRCA2 molecules at DNA damage for
489 a longer period and could explain the motion patterns observed for BRCA2.

490 A similar mechanism could operate within a focus. Our observation by single-molecule
491 localization microscopy (**Figure 3**) of BRCA2 clusters within a focus suggests that the
492 chromatin environment within a focus is not homogeneous. The measured distance between
493 these intra-focus BRCA2 clusters (**Figure 3**) is consistent with the possibility of displacement
494 of BRCA2 molecules between these clusters (resulting in the class of BCRA2 molecules with
495 confined motion), while molecules with larger displacements would lose their association
496 with the clusters. It remains to be investigated what interactions drive these motion patterns,
497 but it should be considered that BRCA2 is present in complex with several other repair
498 proteins such as PALB2 and RAD51. For example, loss of the PALB2-BRCA2 interaction
499 prevents BRCA2 localization in foci (9). On the contrary, the accumulation of BRCA2 does not
500 depend on its highly conserved DNA binding domain and the C-terminal domain (8), which,
501 at least in vitro, interact with (single-stranded) DNA (28). An explanation is that BRCA2 is
502 bound to chromatin surrounding the DNA damage mainly through its N-terminal interaction
503 with PALB2, without the requirement of all functional domains required to promote all
504 BRCA2 functions. In this way, the accumulation of BRCA2 is uncoupled from its canonical
505 function of loading RAD51 onto RPA coated DNA. On the other hand, the transient
506 interactions will help BRCA2 to reside at a focus for longer, that might be required to give
507 BRCA2 sufficient time to exert its function of regulating RAD51 filament formation.

508 **Mechanisms of accumulation of BRCA2 at DNA lesions**

509 The dynamics of a larger number of different DNA repair proteins has been investigated in
510 living cells. It shows that while many of these proteins accumulate at sites of DNA damage,
511 they can do so through different mechanisms (29). While RAD51 and RPA are stably bound
512 (17, 30), RAD54, another protein in the same DNA repair pathway, shows a different dynamic
513 behaviour (17). Interestingly, while RAD54 visually accumulates in foci, immobilization of the
514 protein is hardly observed, unless its ATP activity is affected (31). In recent years, liquid-liquid
515 phase separation (LLPS) has been proposed as an additional mechanism to drive
516 compartmentalization of proteins in DNA repair foci, as well as in other nuclear and cellular

517 processes. 53BP1 is one of the DNA repair factors that forms accumulations with liquid-like
518 characteristics (25, 26). Furthermore, RAD52, a RAD51 mediator in yeast, can form
519 condensates *in vitro* and *in vivo* (32). Another study using single-molecule tracking showed
520 that RAD52 in budding yeast shows reduced and confined mobility in foci, while the RPA
521 subunit Rfa1, shows clear immobilization (30). To drive the formation of condensates
522 proteins need to be present at a high enough concentration, however BRCA2 is present at a
523 low concentration in the cell nucleus and within the foci only tens of BRCA2 molecules are
524 present (**Figure 3**). This suggests that BRCA2 by itself is not phase separated but is trapped
525 in DNA lesion-containing compartments where it undergoes transient immobilization
526 through interaction with other proteins or DNA in the foci. As the examples above show,
527 repair factors can accumulate through different mechanisms of which transient binding and
528 the formation of phase separated compartments are the most well- described mechanisms.
529 Differentiating between these different modes of accumulation is not straightforward and
530 many different parameters have been proposed to prove the formation of condensates
531 through liquid-liquid phase separation (33). With the current data on BRCA2 mobility we are
532 not able to apply modelling of the different models as we lack accurate information on the
533 strength and reversibility of the binding of BRCA2 within the foci, nor do we have an
534 accurate estimation of the surface potential in a phase-separation model (34).

535 Through different approaches of analysing our tracking data we do observe that the
536 diffusion rate of the diffusive fraction of BRCA2 is not affected inside the repair focus. If
537 BRCA2 would be accumulating through interactions driven by the presence of phase
538 separation, a change in the measured diffusion rate of the diffusing molecules due to
539 transient molecular interactions would be expected, as has been observed for RAD52 in
540 yeast. Simultaneously we observe an increase in subdiffusive motion in the repair foci,
541 however using the mean-square displacement curve of the diffusive molecules we are not
542 able to observe a clear plateau in the MSD curve and the fitted confinement radius does not
543 match the size of repair foci. This suggests that the mobility of BRCA2 is not restricted by the
544 boundary of the focus, but that transient binding contributes to the accumulation of BRCA2.

545 **Dynamic organization of BRCA2 at DNA repair foci**

546 In line with our previous publication on the localization of BRCA2 using antibodies, BRCA2-
547 HaloTag is localized in small clusters at DNA break sites in fixed cells. Quantification of the

548 amount of BRCA2 in cell nuclei and repair foci specifically shows that only tens of BRCA2
549 molecules are present in DNA repair foci; therefore, individual clusters of BRCA2 within a
550 focus will contain only a few BRCA2 molecules (**Figure 3**). The emerging picture from several
551 studies that use super resolution microscopy to study the architecture of DNA repair foci is
552 that proteins organized in repair foci in specific patterns rather than a homogeneous mix of
553 different repair factors (35–37). For example, by single-molecule localization microscopy, we
554 have observed that part of the RAD51 proteins that are present at repair foci do not localize
555 with BRCA2 (23). It is interesting to consider that even for proteins that are suggested to
556 accumulate by LLPS, such as 53BP1, there is still spatial inhomogeneity of the protein within
557 the focus, instead of a homogeneous distribution of protein. A challenge for future studies
558 will be to converge the observed mobility patterns of the different proteins with their
559 nanoscale localization at foci. An important aspect that still needs to be addressed is how
560 dynamic the overall organization of repair foci is over time. Future studies using super-
561 resolution microscopy in living cells using methods to enhance spatial and temporal
562 resolution, will hopefully allow to further delineate the significance of spatiotemporal
563 dynamics of DNA repair foci that protect the cells against genomic instability.

564

565 **DATA AVAILABILITY**

566 Source data is deposited at the Zenodo repository. Original images of the tracking
567 experiments can be found at: http://doi.org/10.5281/zenodo.10144073 Source data of other
568 experiments can found at: http://doi.org/10.5281/zenodo.8143173

569

570 **AUTHOR CONTRIBUTIONS**

571 MWP, JA, TLC, RK, and CW designed research; MWP, AT and JA performed research; MWP, JA, EW,
572 HK, RvG and IS contributed new reagents/analytic tools; MWP, JA, EW, HK, RvG, and IS analysed
573 data; MWP, RK and CW wrote the paper. All authors discussed the results and commented on the
574 manuscript.

575

576 **ACKNOWLEDGEMENTS**

577 The authors would like to dedicate this work to our friend and colleague Claire Wyman, who
578 passed away during completion of this research. Aberration corrected multifocal microscopy
579 (acMFM) was performed in collaboration with the Advanced Imaging Center at Janelia
580 Research Campus, a facility jointly supported by the Gordon and Betty Moore Foundation
581 and the Howard Hughes Medical Institute. We thank the Optical Imaging Centre at the
582 Erasmus MC for use and technical assistance with the optical microscopes. We thank the
583 Josephine Nefkens Cancer Program for infrastructure support.

584 **FUNDING**

585 The experimental visit to Janelia was supported by a Journal Cell Science travel grant. This
586 study was supported by the Oncode Institute, which is partly financed by the Dutch Cancer
587 Society.

588

589 **CONFLICT OF INTEREST**

590 All authors declare that they have no conflicts of interest.

591 **REFERENCES**

592 1. Paul,M.W., Sidhu,A., Liang,Y., van Rossum-Fikkert,S.E., Odijk,H., Zelensky,A.N., Kanaar,R. and
593 Wyman,C. (2021) Role of BRCA2 DNA-binding and C-terminal domain on its mobility
594 and conformation in DNA repair. *eLife*, **10**, e67926.

595 2. Reuter,M., Zelensky,A., Smal,I., Meijering,E., van Cappellen,W.A., de Gruiter,H.M., van
596 Belle,G.J., van Royen,M.E., Houtsmuller,A.B., Essers,J., *et al.* (2014) BRCA2 diffuses as
597 oligomeric clusters with RAD51 and changes mobility after DNA damage in live cells.
598 *The Journal of Cell Biology*, **207**, 599–613.

599 3. Zelensky,A.N., Schimmel,J., Kool,H., Kanaar,R. and Tijsterman,M. (2017) Inactivation of Pol θ
600 and C-NHEJ eliminates off-target integration of exogenous DNA. *Nature*
601 *Communications*, **8**.

602 4. Yang,K.S., Kohler,R.H., Landon,M., Giedt,R. and Weissleder,R. (2015) Single cell resolution in
603 vivo imaging of DNA damage following PARP inhibition. *Scientific Reports*, **5**, 10129.

604 5. Abrahamsson,S., Chen,J., Hajj,B., Stallinga,S., Katsov,A.Y., Wisniewski,J., Mizuguchi,G.,
605 Soule,P., Mueller,F., Darzacq,C.D., *et al.* (2013) Fast multicolor 3D imaging using
606 aberration-corrected multifocus microscopy. *Nature Methods*, **10**, 60–63.

607 6. Bohrer,C.H., Yang,X., Thakur,S., Weng,X., Tenner,B., McQuillen,R., Ross,B., Wooten,M.,
608 Chen,X., Zhang,J., *et al.* (2021) A pairwise distance distribution correction (DDC)
609 algorithm to eliminate blinking-caused artifacts in SMLM. *Nat Methods*, **18**, 669–677.

610 7. Sbalzarini,I.F. and Koumoutsakos,P. (2005) Feature point tracking and trajectory analysis for
611 video imaging in cell biology. *J. Struct. Biol.*, **151**, 182–195.

612 8. Arts,M., Smal,I., Paul,M.W., Wyman,C. and Meijering,E. (2019) Particle Mobility Analysis
613 Using Deep Learning and the Moment Scaling Spectrum. *Sci Rep*, **9**, 1–10.

614 9. Ushey,K., Allaire,J.J. and Tang,Y. (2019) reticulate: Interface to 'Python'.

615 10. Metzler,R., Jeon,J.-H., Cherstvy,A.G. and Barkai,E. (2014) Anomalous diffusion models and
616 their properties: non-stationarity, non-ergodicity, and ageing at the centenary of
617 single particle tracking. *Phys. Chem. Chem. Phys.*, **16**, 24128–24164.

618 11. Lerner,J., Gómez-García,P.A., McCarthy,R.L., Liu,Z., Lakadamyali,M. and Zaret,K.S. (2020)
619 Two-parameter single-molecule analysis for measurement of chromatin mobility.
620 *STAR Protocols*, **1**, 100223.

621 12. Ershov,D., Phan,M.-S., Pylvänäinen,J.W., Rigaud,S.U., Le Blanc,L., Charles-Orszag,A.,
622 Conway,J.R.W., Laine,R.F., Roy,N.H., Bonazzi,D., *et al.* (2022) TrackMate 7: integrating
623 state-of-the-art segmentation algorithms into tracking pipelines. *Nat Methods*, **19**,
624 829–832.

625 13. Pike,J.A., Khan,A.O., Pallini,C., Thomas,S.G., Mund,M., Ries,J., Poulter,N.S. and Styles,I.B.
626 (2020) Topological data analysis quantifies biological nano-structure from single
627 molecule localization microscopy. *Bioinformatics*, **36**, 1614–1621.

628 14. Paul,M.W., de Gruiter,H.M., Lin,Z., Baarends,W.M., van Cappellen,W.A., Houtsmuller,A.B.
629 and Slotman,J.A. (2019) SMoLR: visualization and analysis of single-molecule
630 localization microscopy data in R. *BMC Bioinformatics*, **20**.

631 15. Schmidt,U., Weigert,M., Broaddus,C. and Myers,G. (2018) Cell Detection with Star-convex
632 Polygons. *arXiv:1806.03535 [cs]*, **11071**, 265–273.

633 16. McQuin,C., Goodman,A., Chernyshev,V., Kamentsky,L., Cimini,B.A., Karhohs,K.W., Doan,M.,
634 Ding,L., Rafelski,S.M., Thirstrup,D., *et al.* (2018) CellProfiler 3.0: Next-generation image
635 processing for biology. *PLOS Biology*, **16**, e2005970.

636 17. Aaron,J., Wait,E., DeSantis,M. and Chew,T. (2019) Practical Considerations in Particle and
637 Object Tracking and Analysis. *Current Protocols in Cell Biology*, 10.1002/cpcb.88.

638 18. Essers,J., Houtsmuller,A.B., van Veelen,L., Paulusma,C., Nigg,A.L., Pastink,A., Vermeulen,W.,
639 Hoeijmakers,J.H.J. and Kanaar,R. (2002) Nuclear dynamics of RAD52 group
640 homologous recombination proteins in response to DNA damage. *EMBO J*, **21**, 2030–
641 2037.

642 19. Krawczyk,P.M., Borovski,T., Stap,J., Cijsouw,T., Cate,R. t., Medema,J.P., Kanaar,R.,
643 Franken,N.A.P. and Aten,J.A. (2012) Chromatin mobility is increased at sites of DNA
644 double-strand breaks. *Journal of Cell Science*, **125**, 2127–2133.

645 20. Dimitrova,N., Chen,Y.-C.M., Spector,D.L. and Lange,T. de (2008) 53BP1 promotes non-
646 homologous end joining of telomeres by increasing chromatin mobility. *Nature*, **456**,
647 524–528.

648 21. Lottersberger,F., Karssemeijer,R.A., Dimitrova,N. and de Lange,T. (2015) 53BP1 and the
649 LINC Complex Promote Microtubule-Dependent DSB Mobility and DNA Repair. *Cell*,
650 **163**, 880–893.

651 22. Hansen,A.S., Amitai,A., Cattoglio,C., Tjian,R. and Darzacq,X. (2019) Guided nuclear
652 exploration increases CTCF target search efficiency. *Nat Chem Biol*, 10.1038/s41589-
653 019-0422-3.

654 23. Izeddin,I., Récamier,V., Bosanac,L., Cissé,I.I., Boudarene,L., Dugast-Darzacq,C., Proux,F.,
655 Bénichou,O., Voituriez,R., Bensaude,O., *et al.* (2014) Single-molecule tracking in live
656 cells reveals distinct target-search strategies of transcription factors in the nucleus.
657 *eLife*, **3**.

658 24. Sánchez,H., Paul,M.W., Grosbart,M., van Rossum-Fikkert,S.E., Lebbink,J.H.G., Kanaar,R.,
659 Houtsmuller,A.B. and Wyman,C. (2017) Architectural plasticity of human BRCA2–
660 RAD51 complexes in DNA break repair. *Nucleic Acids Research*, **45**, 4507–4518.

661 25. Kilic,S., Lezaja,A., Gatti,M., Bianco,E., Michelena,J., Imhof,R. and Altmeyer,M. (2019) Phase
662 separation of 53BP1 determines liquid-like behavior of DNA repair compartments.
663 *The EMBO Journal*, **0**, e101379.

664 26. Pessina,F., Giavazzi,F., Yin,Y., Gioia,U., Vitelli,V., Galbiati,A., Barozzi,S., Garre,M., Oldani,A.,
665 Flaus,A., *et al.* (2019) Functional transcription promoters at DNA double-strand breaks
666 mediate RNA-driven phase separation of damage-response factors. *Nat Cell Biol*, **21**,
667 1286–1299.

668 27. Alexander,J.M., Guan,J., Li,B., Maliskova,L., Song,M., Shen,Y., Huang,B., Lomvardas,S. and
669 Weiner,O.D. (2019) Live-cell imaging reveals enhancer-dependent Sox2 transcription
670 in the absence of enhancer proximity. *eLife*, **8**, e41769.

671 28. Liu,Z., Legant,W.R., Chen,B.-C., Li,L., Grimm,J.B., Lavis,L.D., Betzig,E. and Tjian,R. (2014) 3D
672 imaging of Sox2 enhancer clusters in embryonic stem cells. *eLife*, **3**.

673 29. Xia,B., Sheng,Q., Nakanishi,K., Ohashi,A., Wu,J., Christ,N., Liu,X., Jasin,M., Couch,F.J. and
674 Livingston,D.M. (2006) Control of BRCA2 Cellular and Clinical Functions by a Nuclear
675 Partner, PALB2. *Molecular Cell*, **22**, 719–729.

676 30. Yang,H. (2002) BRCA2 Function in DNA Binding and Recombination from a BRCA2-DSS1-
677 ssDNA Structure. *Science*, **297**, 1837–1848.

678 31. Miné-Hattab,J., Liu,S. and Taddei,A. (2022) Repair Foci as Liquid Phase Separation:
679 Evidence and Limitations. *Genes*, **13**, 1846.

680 32. Miné-Hattab,J., Heltberg,M., Villemeur,M., Guedj,C., Mora,T., Walczak,A.M., Dahan,M. and
681 Taddei,A. (2021) Single molecule microscopy reveals key physical features of repair
682 foci in living cells. *eLife*, **10**, e60577.

683 33. Agarwal,S., van Cappellen,W.A., Guénolé,A., Eppink,B., Linsen,S.E.V., Meijering,E.,
684 Houtsmuller,A., Kanaar,R. and Essers,J. (2011) ATP-dependent and independent
685 functions of Rad54 in genome maintenance. *The Journal of Cell Biology*, **192**, 735–
686 750.

687 34. Oshidari,R., Huang,R., Medghalchi,M., Tse,E.Y.W., Ashgriz,N., Lee,H.O., Wyatt,H. and
688 Mekhail,K. (2020) DNA repair by Rad52 liquid droplets. *Nat Commun*, **11**, 1–8.

689 35. McSwiggen,D.T., Mir,M., Darzacq,X. and Tjian,R. (2019) Evaluating phase separation in live
690 cells: diagnosis, caveats, and functional consequences. *Genes Dev.*,
691 10.1101/gad.331520.119.

692 36. Heltberg,M.L., Miné-Hattab,J., Taddei,A., Walczak,A.M. and Mora,T. (2021) Physical
693 observables to determine the nature of membrane-less cellular sub-compartments.
694 *bioRxiv*, 10.1101/2021.04.01.438041.

695 37. Chapman,J.R., Sossick,A.J., Boulton,S.J. and Jackson,S.P. (2012) BRCA1-associated
696 exclusion of 53BP1 from DNA damage sites underlies temporal control of DNA repair.
697 *Journal of Cell Science*, **125**, 3529–3534.

698 38. Whelan,D.R., Lee,W.T.C., Yin,Y., Ofri,D.M., Bermudez-Hernandez,K., Keegan,S., Fenyo,D.
699 and Rothenberg,E. (2018) Spatiotemporal dynamics of homologous recombination
700 repair at single collapsed replication forks. *Nature Communications*, **9**, 3882.

701 39. Ochs,F., Karemore,G., Miron,E., Brown,J., Sedlackova,H., Rask,M.-B., Lampe,M., Buckle,V.,
702 Schermelleh,L., Lukas,J., *et al.* (2019) Stabilization of chromatin topology safeguards
703 genome integrity. *Nature*, **574**, 571–574.

704

705

706

707 **MAIN FIGURES**

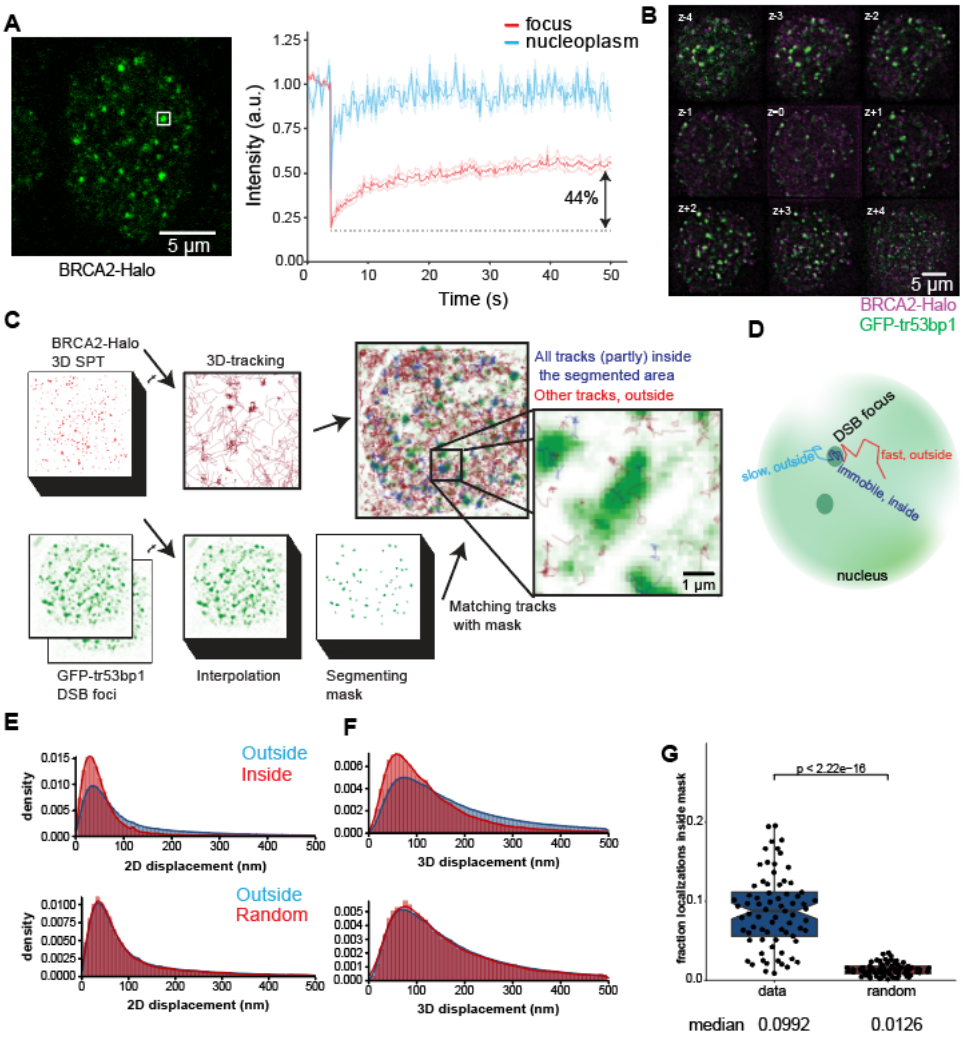

708

709 **Figure 1: Analysis of the mobility of BRCA2 at DNA damage sites. A** Spot-FRAP of
710 BRCA2-HaloTag cells treated with mitomycin C by photobleaching a focus or region in the
711 cytoplasm (3 independent replicates, focus n=40, nucleoplasm n=20 cells, shading around
712 the curve indicates SEM) **B** Example of a single multi-focal plane image showing 9 z-plane
713 projections spaced 420 nm apart; the signal of BRCA2-Halo (magenta) and EGFP-tr53BP1
714 (green) is shown. **C** Approach for analysis of molecule tracks in and outside the foci, by
715 matching the localized molecules to the binary mask of the damage sites defined by the
716 53BP1 signal. **D** All track segments in the data set are annotated as being in or outside the
717 DSB foci and having a fast, slow, or immobile state. **E,F** Distribution of mean x-y (2D) and x-
718 y-z (3D) displacements for track segments outside versus inside the DSB foci mask. The plots
719 below show the distribution but for a random mask. **G** Fraction of localizations in and
720 outside the defined mask for the data compared to the random mask. The data consist of 4

721 independent experiments of 73 cells in total. See Movies S1-3 for movies of this data. p-
722 values are calculated from an unpaired 2-sample Wilcox rank sum test.

723

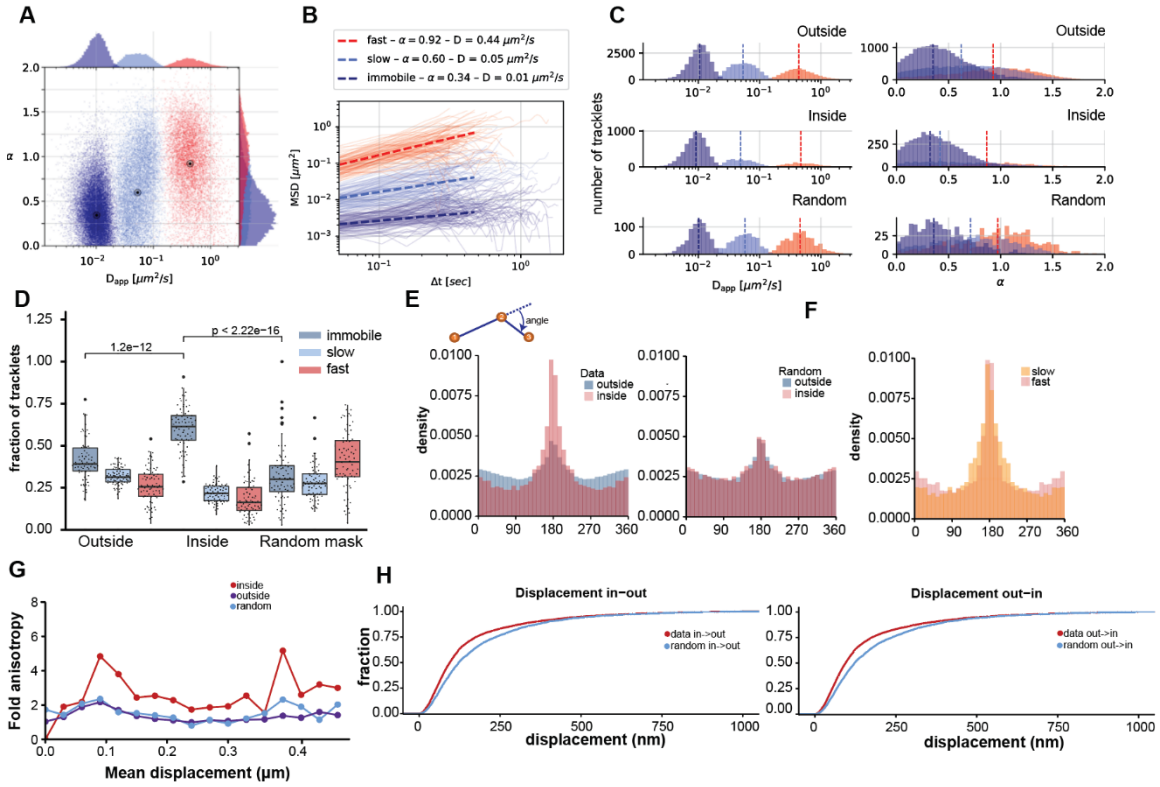

724

725 **Figure 2: In-depth analysis of mobility in and outside the foci. A** Scatter plot showing the
726 estimated apparent diffusion constant (Dapp) and anomalous exponent (α) distribution of
727 immobile (blue, Dapp: 0.01 μm2/s, α: 0.34), slow (light blue, Dapp: 0.053, α: 0.60) and fast
728 (red, Dapp: 0.43, α: 0.93) tracklets of BRCA2-HaloTag in mitomycin C treated cells. The black
729 points in the plot indicate the median values for each cluster. **B** For each diffusive state,
730 example of 100 MSD lines with the MSD fit using the power law equation and the medians
731 Dapp and α values. **C** The distribution of Dapp and α values per tracklet outside (Dapp:
732 0.43;0.05;0.01 μm2/s, α: 0.93;0.62;0.35) , inside (Dapp: 0.42;0.05;0.01 μm2/s, α: 0.87;0.41;0.32)
733 and inside the random mask (Dapp: 0.46;0.06;0.01 μm2/s, α: 0.97;0.71;0.36). The histograms
734 display the overall distribution of all cells imaged. **D** Quantification of the distribution of
735 tracklets outside, inside and inside random mask. The indicated fraction is estimated from
736 the mean fraction per cell. **E** Angular distributions calculated between subsequent
737 localizations. Displacements of immobile molecules are excluded from the analysis. The
738 determined distribution of angles for BRCA2 is plotted for all molecules outside and inside

739 the damage site and compared to a randomized mask. **F** Angular distribution of fast and
740 slow-moving molecules **G** Distribution of the fold anisotropy (ratio between backward angle
741 (180 +/- 15 degrees) versus forward angle (0 +/- 15 degrees) plotted against mean
742 displacement of the track. **H** Cumulative distribution of the displacements of the track
743 segments that transition from inside to outside (left) and from outside to inside (right) of the
744 foci, where immobile molecules are excluded from the distribution. Analysis in this figure is
745 done in 2D using the x-y coordinates in the tracking data. The data consists of four
746 independent experiments of 73 cells in total. p-values are calculated from an unpaired 2-
747 sample Wilcox rank sum test.

748

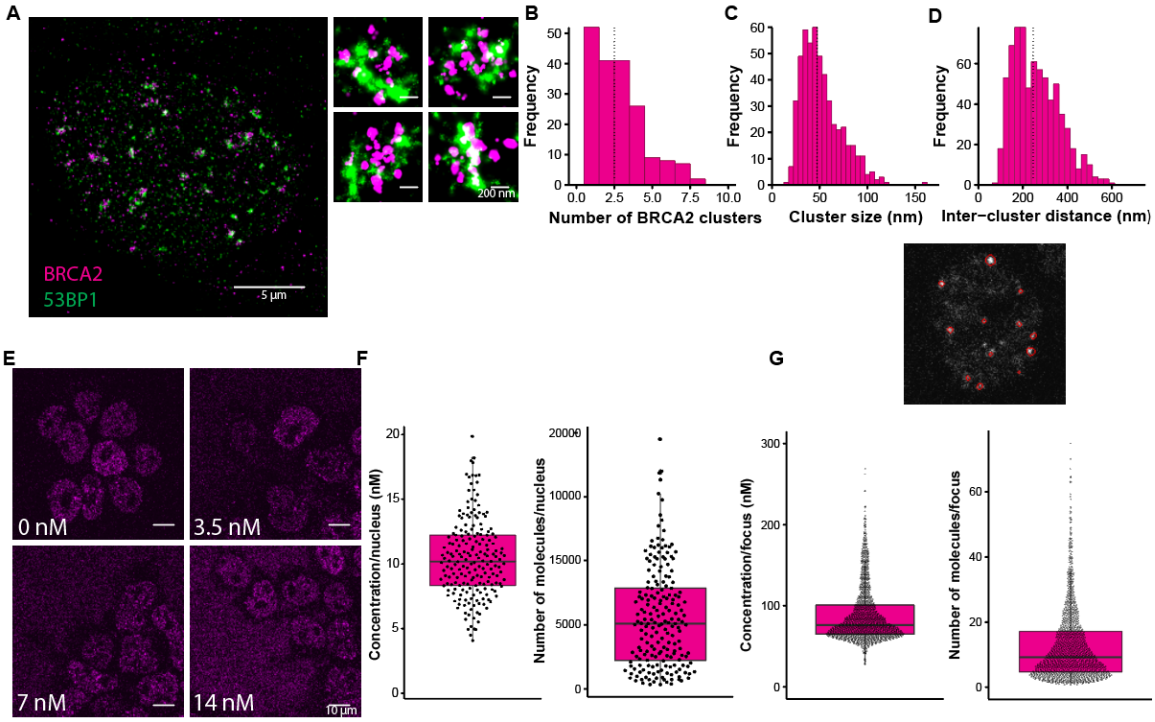

749

750 **Figure 3: Nanoscale localization of BRCA2 in MMC-induced DNA repair foci and**
751 **quantification of nuclear BRCA2 concentration. A** Two-color dSTORM image of BRCA2-
752 Halo::Alexa647 and 53BP1 (indirect immunofluorescence CF568). Typical examples of foci
753 with both BRCA2 and 53bp1 signal. **B** Quantification of the number of BRCA2 clusters within
754 individual automatically segmented 53BP1 foci. **C-D** Quantification of the size of the
755 respective clusters and the centre-to-centre distance between the clusters within the
756 individual foci. Data from 7 cells in total from two imaging sessions. Analysis of 7 images
757 with a total of 189 foci analyzed. Dashed line indicate the median of the distributions. **E** The

758 cellular concentration of BRCA2 was estimated by titration of increasing concentrations of
759 the labeled GST-HaloTag protein in the cell medium. The voxel intensity was used to
760 estimate the local concentration. **F** The nuclear concentration was estimated by 3D
761 segmentation of the cell nuclei. The nuclear concentration is defined as the average nuclear
762 concentration within all voxels in the 3D nuclear volume, whereas the number of BRCA2
763 molecules per nucleus is calculated by multiplying the concentration with the estimated
764 nuclear volume. **G** Within the identified nuclei, the foci were segmented in 3D. The image
765 shows an example of the segmentation in a single confocal slice. The plots show the results
766 of one replicate, results from additional replicates (n=3) are summarized in Fig. S6.